Configuration Tradeoffs for the Space Infrared Telescope Facility Pointing Control System

A. J. Pue,* K. Strohbehn,† and J. W. Hunt‡
The Johns Hopkins University, Applied Physics Laboratory, Laurel, Maryland

Candidate pointing control configurations for a Space Infrared Telescope Facility are examined in terms of fine guidance pointing and large angle slewing accuracies. In particular, the fundamental tradeoff is between a strategy that uses body pointing only, where the entire spacecraft is controlled to null pointing error, or body pointing plus image motion compensation, where a movable secondary mirror is employed to remove high-frequency disturbances and therefore mitigate excitation of flexible body modes. Using known characteristics of available attitude control sensors and actuators, a linear covariance analysis is used to compute rms pointing error, while a time domain simulation is used to compute transient response to specific disturbance torques. It is found that body pointing alone can provide excellent fine pointing accuracy but limits slewing performance. Both slewing performance and disturbance rejection may be significantly improved by a steerable secondary mirror, but the noise level of the attitude sensor under study limits control bandwidth and thus restricts the potential advantages of this approach. It is recommended that improved sensor designs be pursued while enhancing slewing performance by appropriate combination of command profile and control compensation.

I. Introduction

THE Space Infrared Telescope Facility (SIRTF) is a 1-m class, cryogenically cooled, IR astronomical observatory required to have an image stability of 100 milliarcsec rms at the focal plane. Initially, it was planned that SIRTF be attached to the Space Shuttle via a gimbal system. But, with the success of the Infrared Astronomy Satellite (IRAS) and because of concern over contamination of the optical system by the shuttle environment, the SIRTF design has been changed to a free-flying spacecraft.[1] A consequence of this change is that a pointing control system (PCS) must be defined. In particular, a central issue is the tradeoff between body pointing, where attitude sensor and gyro measurements are used to torque the entire spacecraft, and body pointing plus image motion compensation (IMC), where a steerable secondary mirror is used to remove high-frequency disturbances.

The primary objective of this study was to explore conceptual pointing control system designs and to assess overall system pointing performance vs control system configuration via analysis and time domain simulation. More specifically, the objectives were to 1) identify candidate control laws, sensors, and actuators, 2) investigate the tradeoffs between control methodologies, sensor accuracies, and pointing performance, and 3) investigate the impact of control design on flexible mode suppression during slew maneuvers and in the presence of disturbances. Currently, the requirements are that a large-angle maneuver of 120 deg be accomplished within 8 min and that a 7.5-arcmin slew (nod) be accomplished within 10 s. In addition, signal spatial chopping by articulation of a secondary mirror is specified to be 7.5 arcmin at 20 Hz with a 90% duty cycle.

The analysis of rms pointing stability was based on a steady-state linear covariance analysis, while step responses were used to assess the suppression of flexible modes. A time domain simulation which includes nonlinearities was used to evaluate the transient response to specific disturbance torques.

II. System Modeling

The baseline SIRTF structural model[1] is similar in overall configuration to the Hubble Space Telescope. For the purpose of preliminary control system assessment, simplified models of the actuators, gyros, attitude sensor, and structure were selected. These selections, however, were based on available hardware devices and used their known characteristics. These devices are described below in addition to specific disturbance torque models.

Actuator Selection and Modeling

The baseline requirement to slew 15 deg/min determines the peak torque and momentum an actuator must deliver. For an inertia of 33,700 kg-m^2 and a triangular torque vs time profile, it is found that the actuator must supply 20 N-m of torque and be able to store 300 N-m-s of angular momentum.

A survey[2] of available actuator hardware revealed that only single gimbal control moment gyros could meet the SIRTF requirements. For example, the Sperry SG-CMG model M225 is capable of developing a maximum torque of 300 Nm, produces 300 N-m-s of angular momentum, and has a control bandwidth of 20 Hz.[3]

An important factor to consider in pointing performance is CMG noise caused by vibration. The major sources of CMG vibration are 1) gyroscopic torques caused by gimbal rate due to tachometer, torque motor, gear train, and electronic imperfections, 2) mass unbalance torques, and 3) disturbance torques, and radial and axial forces transferred to the structure through the CMG bearings at constant multiples of the running speed.

Table 1 lists the peak magnitudes of these disturbances for the Sperry M225 SG-CMG. In addition, using techniques successfully applied to the M1300, predicted characteristics of a quieted version are shown. Rate ripple is the dominant CMG-induced disturbance that occurs within the CMG control loop bandwidth. The other CMG disturbances all occur at multiples of the running speed and are therefore typically outside the control loop bandwidth and have not been included in the present analysis.

Presented as Paper 85-1856 at the AIAA Guidance, Navigation and Control Conference, Snowmass, CO, Aug. 19-21, 1985; received Feb. 3, 1986, revision received May 21, 1986.

*Engineer, Fleet Systems Department.

†Engineer, Space Department.

‡Engineer, Space Department. Member AIAA.

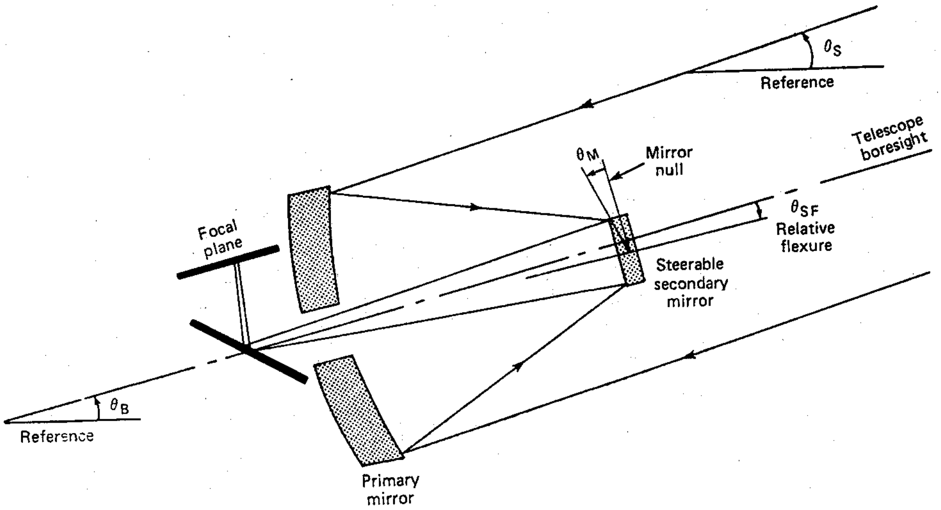

Fig. 1 Optical model diagram.

Sensor Selection and Modeling

The baseline optical configuration for SIRTF is illustrated by the diagram in Fig. 1. A steerable mirror is included for the image motion compensation option, but would be fixed for the body pointing option. The data star of interest is defined at an angle θ_S with respect to a fixed reference, while the telescope boresight (or the boresight of a specific science instrument in the focal plane) is at an angle θ_B with respect to the same fixed reference. Thus, the system error is $\epsilon = \theta_S - \theta_B$. Differences between ϵ and the measured angular error of the image θ_I are caused by the angle of the steerable secondary mirror θ_M with respect to a null, and the relative flexure θ_{SF} of the secondary mirror with respect to the boresight. It is seen that the effect of θ_{SF} on θ_I is equivalent to θ_M (except for translational effects neglected here), and the total effect on θ_I is $2(\theta_M + \theta_{SF})$, assuming there is no additional magnification in the optics other than a flat mirror effect. Finally, flexure of the primary mirror θ_{PF} relative to the boresight causes a distortion, $2\theta_{PF}$. Thus, the measured image is given by

$$\theta_I = K_o(\theta_S - \theta_B - 2\theta_{PF}) + 2(\theta_M + \theta_{SF}) \qquad (1)$$

where K_o is the optical gain and all signs are consistent with positive counterclockwise rotations. (Note that a negative rotation for θ_{SF} is shown in Fig. 1.) Motion of the focal plane due to flexure is included in θ_B as θ_{BF}.

For pointing control, the system does not use the image of the data star, but rather relies on a guide star that is focused onto a sensor in the telescope focal plane. If the guide star is offset from the data star by an angle $\Delta\theta_{GS}$, then from Eq (1) the image of the guide star is at an angle

$$\theta_{IGS} = K_o(\theta_S + \Delta\theta_{GS} - \theta_B - 2\theta_{PF}) + 2(\theta_M + \theta_{SF}) \qquad (2)$$

Dividing by the optical gain, the measured pointing error to the guide star is

$$\epsilon_{GS} = \theta_S + \Delta\theta_{GS} - \theta_B + 2(\theta_m + \theta_{SF})/K_o - 2\theta_{PF} + n_S \qquad (3)$$

where n_S is sensor noise. The baseline attitude sensor was selected to be a charge transfer device (CTD) array.[2] The CTD noise, n_S, is modeled as a zero mean Gaussian random variable with an rms value based on noise equivalent angle (NEA) and nominal integration time T. For the SIRTF simulations, the baseline values $T = 1$ s and NEA = 31.2 milliarcsec were obtained[2] based on work by Kollodge and Sand.[4] Because the pointing performance is nearly linear in NEA, the selection of a reasonable baseline NEA value is not critical. To investigate the relationships between T, IMC bandwidth, and resulting noise level, the rms sensor noise was modeled as $1.5 \times 10^{-7}\ T^{-3/2}$ rad.[2]

Gyro Model

A DRIRU-2 gyro[5] was selected as a baseline attitude rate sensor primarily for its low noise characteristics. It is modeled as a second-order transfer function having a 0.707 damping ratio and 18 Hz natural frequency. The noise power spectral density[5] was used to design the shaping filter

$$H_g(s) = \frac{\omega_2^2[(s/\omega_1) + 1]}{s^2 + 2\zeta\omega_2 s + \omega_2^2}$$

with $\zeta = 1$, $\omega_1 = 15.708$ rad/s, and $\omega_2 = 251.3$ rad/s (white noise input psd $= 2.35 \times 10^{-18}$ (rad/s)^2/Hz/s).

Disturbance Torques

The environmental forces and torques for which the PCS must compensate include gravity-gradient effects, aerodynamic effects, solar pressure effects, and magnetic effects. In general, magnetic torques will exist because of the fixed residual dipoles in the spacecraft elements, dipoles induced in the spacecraft by the local magnetic field, and dipoles deliberately generated in the magnetic torquers for control or momentum dumping. The residual and induced dipoles are typically small, so in this preliminary analysis their effect may be neglected. The magnetic torquers which will be used as a backup control actuator and for occasional momentum dumping have also been neglected.

The standard linearized gravity gradient torque[6] is $T = 3n^2\hat{r} \times (I\hat{r})$ where I is the spacecraft inertia tensor, $\hat{r}$ is the instantaneous local vertical unit vector, and n is the orbital rate (rad/s). This torque will be a function of the spacecraft attitude relative to the rotating local vertical reference frame. The worst case ($\hat{r}$ normal to $I\hat{r}$) gravity gradient torque is $T_G = \frac{3}{2}n^2(I_R - I_Y)$, where I_R and I_Y are the roll and yaw axis moments of inertia, respectively. A 600-km circular orbit and a moment of inertia difference of $I_R - I_Y = 12000$ kg-m^2 have been used to determine $T_G = .021$ N-m.

Table 1 Sperry M225 disturbances (maximum)

	Off-the-shelf version	Quieted version
Static unbalance	13 N	0.4 N
Dynamic unbalance	5.5 N-m	0.12 N-m
Rate ripple	3%	0.5%
Torque ripple	10 N-m	1.5 N-m

Aerodynamic forces and torques were evaluated by modeling the SIRTF external structure using 457 triangular plates composing 20 basic objects (frustums and rectangular pyramids). Forces and torques are calculated for any SIRTF orientation, providing atmospheric temperature and density are known for the given orbit. For the purposes of this study, the Jacchia '77 model[7] was used to find air temperature and density at the nominal altitude of 600 km. A median exospheric temperature of 1000 K was assumed, corresponding to a constant air temperature of 998 K at 600 km (from the static model tables). Mean molecular density is 1.2×10^{-13} kg/m^3 according to the model.

Aerodynamic forces and torques were computed for angle of attack and sideslip in 22.5-deg intervals in the range from 0 to 180 deg inclusive.[2] For the present single-plane analysis, the aerodynamic torque was assumed constant and taken to be the pitch bias torque corresponding to zero angle of attack and sideslip and equal to $T_{\mathrm{aero}} = 1.3 \times 10^{-4}$ N-m.

A number of internal disturbance sources exist which may further degrade SIRTF pointing performance. Pointing of the solar panels or the TDRSS antennas will cause the spacecraft to rotate as angular momentum is exchanged between the spacecraft and the device being rotated. In this case, it may be possible to command the CMG's so that the momentum exchange takes place between the CMG's and the solar panels or antennas. The spacecraft and, more importantly, the telescope line of sight would then not be adversely affected by the appendage orientation maneuver.

Cryogen Effects

The effects of the superfluid, cryogenic helium are difficult to quantify because of the unknown behavior of this liquid in a zero-*g* vacuum. One source of disturbance will occur as the helium is vented after boil-off. Ideally, the helium will be vented through the system center of mass so that no torques will be imposed on the spacecraft. Undoubtedly, the center of mass will not be known accurately enough to remove all torques.

The more important problem, and the least known, involves the fluid dynamics of cryogenic helium as the spacecraft is maneuvered. It is expected that the helium mass at launch will be 625 kg, and thus slosh is a potentially important error source. In a static condition, the superfluid helium will cling to the walls of the Dewar, leaving a toroidal bubble in the middle of the tank. For small motions of the tank, however, the resulting fluid motion is not evident. The only recommendation that can be made at this time is to place as many baffles as possible in the cryogen Dewar to promote accumulation of the helium along the surfaces of the Dewar. This issue may not be resolved until an experiment is placed in orbit to measure the cryogenic motion.

For the purpose of modeling cryogen slosh and ensuring that the control system can attenuate this disturbance, a worst case situation where the helium behaves as a lumped mass oscillating at low frequency was assumed. Specifically, the cryogen is modeled as a rigid pendulum free to rotate about the telescope optical axis. By also allowing the base of the pendulum to translate along the telescope axis, the cryogen is given two degrees of freedom relative to the telescope. Coupling of the cryogen motion with the telescope is done through linear springs and dampers.

Table 2 Flexible body modes

Mode	Frequency, Hz	Damping	Gain	Source
1	0.022	0.035	-3.01×10^{-5} (1/3 full)	Slosh
2	0.100	0.030	-3.598×10^{-4}	Slosh
3	0.545	0.003	4.239×10^{-7}	Solar arrays
4	0.551	0.003	8.657×10^{-6}	Solar arrays
5	0.601	0.003	1.061×10^{-9}	Solar arrays
6	0.648	0.004	-2.359×10^{-4}	Solar arrays
7	1.007	0.008	-3.408×10^{-4}	Solar arrays
8	1.628	0.004	1.708×10^{-5}	TDRSS antennas
9	1.636	0.004	-7.905×10^{-9}	TDRSS antennas
10	1.692	0.004	1.776×10^{-3}	TDRSS antennas

Structural Model

The NASTRAN structural program was used to generate the natural vibration modal characteristics for an 18-degree-of-freedom model consisting of six bodies coupled by five hinges. The frequency, damping ratio, and modal gain for each of the 12 most significant flexible vibration modes are given below in Table 2. In this model, the gyro and all optical elements are affixed to a common rigid body, and therefore, $\theta_{PF} = \theta_{SF} = 0$ in Eq. (1).

To further reduce the complexity of this type model, numerous techniques have been proposed to select the most significant modes. Among these techniques, internal balancing,[8] modal cost analysis,[9] and component cost analysis[10] have been applied to the flexible structure problem. Because component cost analysis is based on a specific design technique, the other two methods were considered. For the simple structural model used, it is found that the two methods produce identical results and correspond to the evaluation of each modal transfer at the modal frequency. That is, for each mode, the quantity $\sigma_i = K_i^2/(2\zeta_i \omega_i^2)$ is computed to represent the gain to the attitude sensor, where ζ_i, ω_i, and K_i are the damping, frequency, and gain for each mode given in Table 2. The gain to the gyro is given by $\omega_i \sigma_i$. Based on this computation, modes 1, 2, 5, 7, and 10 were found to substantially outweigh the remaining modes and were therefore selected for the design and analysis model.

III. Control Configurations

Fundamentally, two control configurations have been investigated, namely, body pointing and image motion compensation. When using body pointing, the image is used to directly control body attitude in conjunction with gyro measurements. When using a steerable mirror, a minor loop is closed so that image motion θ_I may be kept small, although body attitude θ_B may undergo large variation.

Body Pointing

A more detailed diagram of the linear model used for body pointing analysis is shown in Fig. 2. To account for the fact that the attitude sensor measures the guide star image rather than the data star image, we show the measurement to be

$$\epsilon_{GS} = \theta_S + \Delta\theta_{GS} - \theta_B + 2\theta_{SF}/K_o + n_s$$

where $2\theta_{PF}$ in Eq. (1) is combined with θ_B, $\Delta\theta_{GS}$ is the offset of the guide star with respect to the data star, and n_s is sensor noise. To assure the telescope points at the data star rather than the guide star, the control is offset by a command value $\Delta\theta_{GSC}$ which we assume is equal to $\Delta\theta_{GS}$. We will also assume $\theta_S = 0$. We assume that the main structure, less appendages, is rigid, so that for our model, $K_{FS} = K_{FP} = 0$ and $K_{FB} = K_{FG} = K_i$ for each mode.

Finally, included in the diagram are locations of feedforward position, velocity, and acceleration commands (θ_c, $\dot{\theta}_c$, $\ddot{\theta}_c$) and sensor, gyro, and actuator noise.

The baseline control law was selected to emulate the ST control law.[11,12] Thus, it is composed of an observer (also known as a "complementary" filter), PID compensation, and a notch filter. The notch filter is only included to suppress flexible mode disturbances near the control bandwidth.

The observer combines the measurements θ_I at low frequency and $\dot{\theta}_g$ at high frequency to produce the estimated attitude error $\hat{\epsilon}$. That is, the transfer function from θ_I to $\hat{\epsilon}$ is a

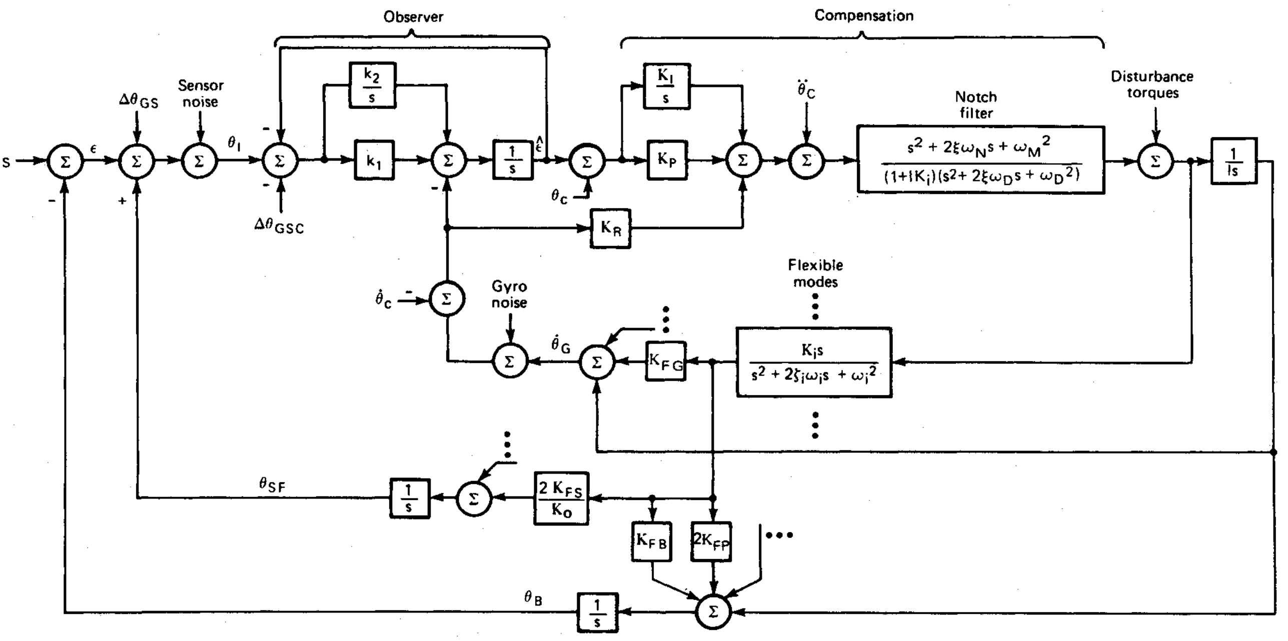

Fig. 2 Pointing control model—body pointing.

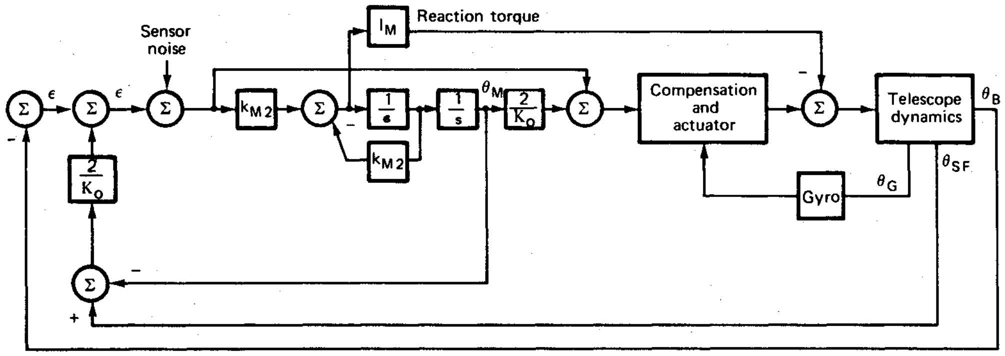

Fig. 3 Pointing control model—image motion compensation.

low-pass filter

$$H_I(s)=\frac{\hat\epsilon(s)}{\theta_I(s)}=\frac{k_1s+k_2}{s^2+k_1s+k_2}$$

while the transfer from $\dot\theta_g$ to $\hat\epsilon$ is a high-pass filter

$$H_g(s)=\frac{\hat\epsilon(s)}{\dot\theta_g(s)}=\frac{s}{s^2+k_1s+k_2}$$

Thus, biases in $\dot\theta_g$ are removed from $\hat\epsilon$, and if $\dot\theta_g\approx\dot\theta_B$, $\theta_I\approx\theta_B$ (neglecting differences in flexure and noise), $\hat\epsilon(s)\approx -H_I(s)\theta_B(s)-H_g(s)\dot\theta_B(s)=-\theta_B(s)$, so $\hat\epsilon$ is an estimate of attitude at all frequencies.

Body Pointing Plus IMC

The basic control configuration for image motion compensation is illustrated in Fig. 3. The body pointing compensation shown in Fig. 2 is assumed to be included in the "compensation" block of Fig. 3. The IMC loop uses the error between the body attitude ϵ and the mirror angle θ_M to torque the mirror in order to null ϵ', the pointing error at the focal plane. A negative sign is assumed within the loop, accounting for the negative feedback shown. The mirror servo is modeled as second-order, with reaction torque $-I_M\ddot\theta_M$ acting on the telescope (I_M = mirror inertia). Notice that the measured value of ϵ' is fed forward to cancel the IMC loop dynamics. Thus, excepting the reaction torque, the open-loop transfer at the actuator is identical to the body pointing, open-loop transfer.

IV. Body Pointing Evaluation

Linear Analysis

We begin with the most basic component of the control law and initially neglect flexible modes to develop relationships between control gains and a selected design bandwidth. The resulting control will then be evaluated, including all elements of the linear model shown in Fig. 2. An excellent report describing some fundamental considerations for body pointing is by D. J. Chiarappa.[13]

The closed-loop dynamics of the body pointing configuration are largely determined by the gains K_R and K_P, while K_I provides low-frequency gain to attenuate low-frequency disturbances. Therefore, temporarily assuming $K_I=0$, the characteristic polynomial is $a(s)=Is^2+K_Rs+K_P$. Letting ω_B be the natural frequency or "design bandwidth," then for a damping ratio of $\zeta=.707$, we have $K_R=1.414\ I\omega_B$ and $K_P=I\omega_B^2$. The crossover frequency of the attitude loop with $K_I=0$ is found by solving $|K_P/[s(sI+K_R)]|_{s=j\omega}=1$ for ω, giving $\omega_C = \omega_B(\sqrt{2} - 1)^{1/2}$. If we now include K_I and select the corner frequency K_I/K_P to be .1 ω_C so as to not significantly affect ω_C, we have $K_I = .06436\ I\omega_B$.[13]

In the presence of the attitude sensor, actuator, and gyro noise sources defined above, a steady-state covariance of the linear model *without* the observer was computed. The rms pointing error in milliarcseconds is plotted in Fig. 4 as a function of design bandwidth, a minimum being reached at $\omega_B = 3$ rad/s, with a 35 marcsec rms pointing error.

To evaluate the effect of including the observer, we first note that a primary function of the attitude observer is to remove gyro bias. Thus, we choose the settling time of the observer as a design parameter to indicate how quickly bias may be initially removed and scientific observation begun. Defining settling time as 4 time constants or $t_s = 4/\zeta\omega_n$ and letting $\zeta = 1$, we have $\omega_n = 4/t_s$. Substituting into $k_1 = \omega_n^2$ and $k_2 = 2\omega_n$ yields $k_1 = 16/t_s^2$ and $k_2 = 8/t_s$.

The tradeoff between settling time and steady-state pointing performance is illustrated by the plot of rms pointing error vs design bandwidth and settling time shown in Fig. 4. Increased settling time produces a reduced rms pointing error but delays initiation of scientific observation. A second consequence of increased settling time is a lengthened response time to disturbances detected by the attitude sensor but not the gyros. An example of this type of disturbance is a boresight shift due to thermal distortion. In this event, restoration of fine pointing is directly related to the settling time of the observer.

Higher values of sensor noise produce a larger rms pointing error in direct proportion. For example, a design bandwidth of $\omega_B = 4$ rad/s with $t_s = 10s$ produces a nominal rms pointing error of 25 marcsec, and thus the sensor rms noise may be increased fourfold before the requirement is violated. Sensitivity to gyro noise, on the other hand, was found to be smaller.[2] A tenfold increase in gyro noise level produces only a 20% increase in rms pointing error.

A second quantity of interest is the control noise at the actuator. The larger the control noise, the greater the potential for actuator saturation, and in addition, greater control energy tends to excite flexible modes. The rms control noise was found to increase linearly with design bandwidth[2] but was less than .1 N-m rms for $\omega_B < 10$ rad/s, and therefore is not a significant factor.

Time Domain Simulation

A time domain simulation was developed to examine transient maneuver performance and the effects of certain disturbance torques. The simulation modeled the linear dynamics shown in Fig. 2 but used discrete time processing at 25 Hz and included a nonlinear CMG noise model (with rate ripple as a function of commanded torque) and torque limit.

A sample time history of pointing error is shown in Fig. 5. A 100-s run was found to be adequate for computing representative rms pointing error values.

This simulation was used to examine the sensitivity of fine pointing performance to the assumed structural model, CMG rate ripple torque level, chopping and nodding torques, and finally, torque caused by science instrument motion such as the Space Telescope high resolution spectrograph (HRS) carousel torque. This latter disturbance was modeled as a 0.353 N-m torque pulse lasting 0.5 s.

To evaluate sensitivity to the structural model, four cases were examined. First, the 0.1-Hz slosh mode was increased by a factor of 10 in gain, lowered to 0.01 Hz, and then removed entirely. No change in rms pointing accuracy was observed. Replacing the SIRTF structural model with the Space Telescope structural model increased the rms pointing error from 9 marcsec to 10 marcsec.

Increasing the CMG rate ripple level from 0.5 to 3% produced no change in rms pointing error. Chopping torque caused by secondary mirror articulation also had no effect on pointing stability.[2] The effect of the HRS carousel torque is an 80-marcsec spike in pointing error lasting approximately 3 seconds.

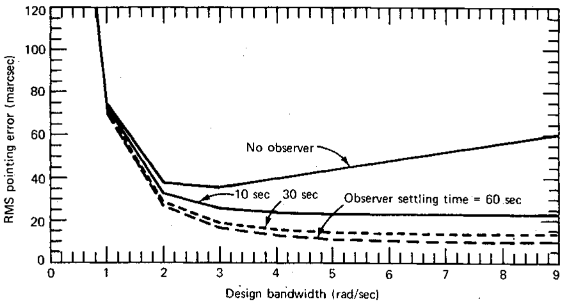

Fig. 4 RMS pointing error vs design bandwidth.

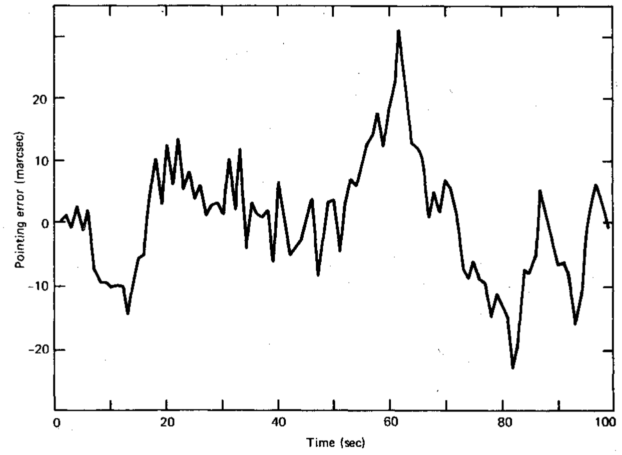

Fig. 5 SIRTF baseline pointing time history.

Slew Maneuver Performance

The most difficult aspect of pointing control is the performing of rapid slew maneuvers and settling within pointing requirements in the face of structural flexibility. Work in the area of large flexible structures, however, has emphasized stability and model reduction.[14] Moreover, studies devoted to precision pointing and slewing have depended on either distributed sensors and actuators[15] or complex optimization algorithms resulting in open-loop controls.[16]

The most conventional and straightforward means of suppressing flexible modes that are near the control bandwidth is notch filtering. Using the configuration shown in Fig. 2, a notch was set at the antenna mode of 10.63 rad/s. The damping ratio was widened to $\zeta = 0.1$ to account for modeling uncertainties.

To evaluate the suppression of the flexible mode, a closed-loop step response was used. We note that a step command in angle is a severe disturbance and primarily serves as a test signal for comparison purposes. In practice, a more gentle taper of feedforward position, velocity, and acceleration commands may be preferred, although if "rapid" slew and acquisition are desired, a step response is indicative of expected performance.

A plot of pointing error after 10 s caused by a 7-arcmin step in angle is shown in Fig. 6. The antenna mode is still present and the 0.1-Hz slosh mode is quite evident. Relative to the performance specification, the response is unsatisfactory. Apparently, additional notch filtering is needed but will create attendant difficulties associated with lag vs design bandwidth and modeling uncertainty.

Thus, rather than pursuing this method, the quadratic regulator approach was examined. To bound the best performance to be expected, full state feedback was initially assumed which, in theory, permits relocation of all modes to give suitable damping. However, this would require large gains and high bandwidth, a risky design in view of model uncertainty. Consequently, only designs which are bandwidth limited were considered.

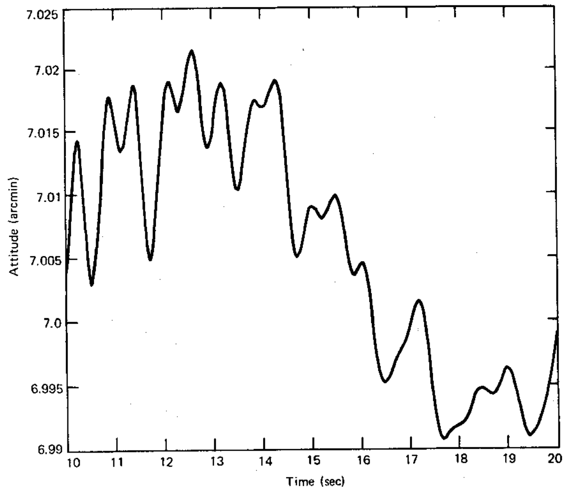

Fig. 6 Step response—notch filtering.

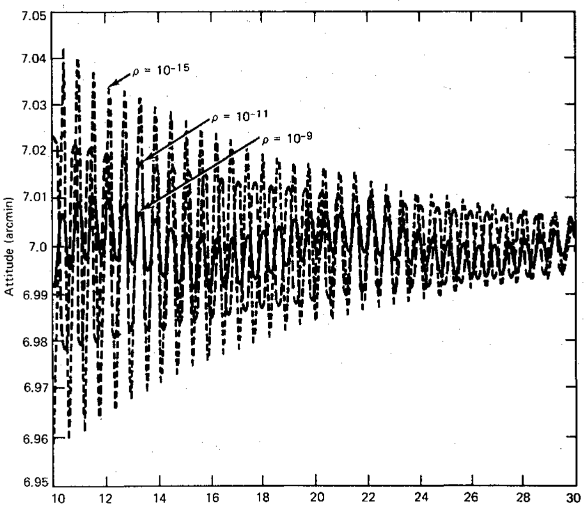

Fig. 7 Expanded time response for LQR design.

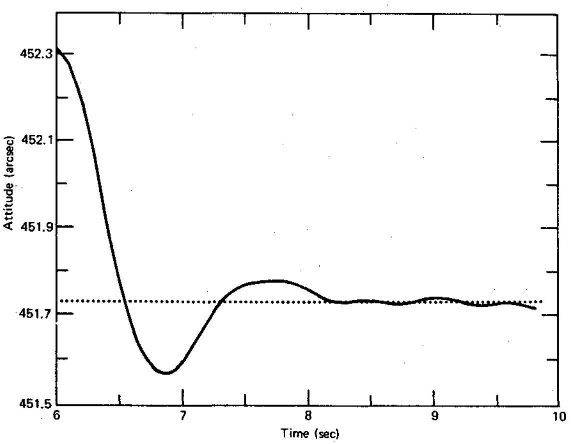

Fig. 8 Attitude response to torque rate limited command profile.

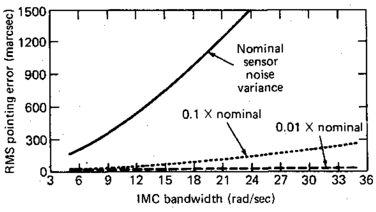

Fig. 9 RMS pointing error for IMC as a function of sensor noise level.

The most basic and simplest LQR design is based on a performance index given by $J = \int_0^\infty [y^2(t) + \rho u^2(t)]dt$ where y is the telescope attitude, u is the control torque, and ρ is the adjustable scalar parameter. The smaller the value ρ, the higher the controller bandwidth.

The plot for step responses after 10 seconds, with ρ adjusted to give loop bandwidth in the range of values we have considered (3-5 rad/s), is shown in Fig. 7. The high bandwidth designs cause greater excitation of the antenna mode but also damp out more rapidly. The lower bandwidth design produces lower excitation at 10 s but is also less effective in damping both the slosh and antenna modes. In any case, the specification is not met.

Alternative LQR designs based on the selection of a state weighting matrix in the performance index were also attempted.[2] Generally, it was found that a single mode (either slosh or antenna) could be effectively suppressed by the appropriate location of zeros, but the overall response was still not satisfactory in terms of the specification.

Reduction in flexible mode excitation may be obtained by a gentle taper of an open-loop torque command, followed by the closure of the precision pointing control loop at the computed maneuver complete time. Although this approach will ultimately constrain slew maneuver time, the time at which pointing accuracy is achieved may actually be shortened. For example, using a piecewise linear sawtooth torque command profile, a 7-arcmin slew response is shown in Fig. 8. The pointing accuracy requirement is achieved after 7.5 s.

V. Image Motion Compensation

The image motion compensation configuration shown in Fig. 3 includes the body pointing design of the previous section. The IMC gains are chosen to be $k_{M1} = \omega_m^2 K_o/2$ and $k_{M2} = 1.4\omega_m$ where the IMC bandwidth ω_m is the design parameter.

The attitude sensor rms noise level is also adjusted according to $n_o T^{-3/2}$ where $n_o = 1.5 \times 10^{-7}$ rad/sec$^{3/2}$. To assure satisfactory stability of the IMC loop, T is selected as $T = 2\pi/(6\omega_m)$.

A plot of rms pointing error vs IMC bandwidth is shown in Fig. 9. The nominal noise level clearly produces unsatisfactory performance in the 3-5 Hz IMC bandwidth range. An effective IMC bandwidth would need to be at least in the 3-5 Hz range to reduce the 1.7 Hz antenna bending mode. Reducing the sensor noise level to $n_o/10$ and $n_o/100$ while maintaining the sample rate dependency shows that a factor of 100 reduction in NEA is needed to obtain reasonable performance.

An alternative IMC implementation is to use the gyro via the observer to control the steerable mirror. An implementation of this form is shown in Fig. 10. The measured value ϵ_m of telescope pointing error ϵ is obtained by adding $2\theta_m/K_o$ to the attitude sensor measurement. This quantity is combined with the gyro measurement to produce an estimated attitude error $\hat{\epsilon}$. Subtracting $2\theta_m/K_o$ from $\hat{\epsilon}$ produces the estimated value of ϵ', termed $\hat{\epsilon}'$, and is used to steer the mirror. As in previous configurations, $\hat{\epsilon}$ is used to control the telescope.

Using this configuration, IMC can effectively remove disturbances that are detected by the gyro. For example, the

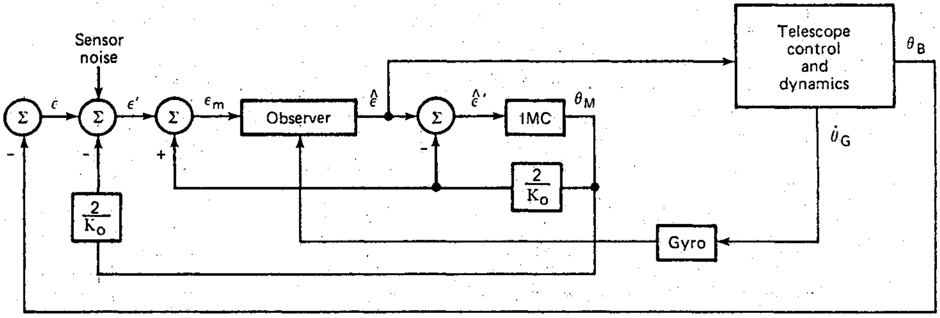

Fig. 10 Alternative IMC implementation.

pointing error spike caused by science instrument torque is reduced from an 80-marcsec peak to a 20-marcsec peak. A similar concept has been employed by Sridhar, Aubrun, and Lorell[17] in an SIRTF pointing control design study. The difficulty in this approach, however, is that the two sensors may be subject to different disturbances (boresight shift, relative secondary-primary mirror flexure). In this event, the attitude sensor is the preferred measurement device.

VI. Conclusions

Results indicate that the SIRTF requirements can be met utilizing available attitude control system sensors and devices that employ proven control techniques.

However, the results do not give a definite choice between body pointing and body pointing plus secondary mirror control. Body pointing can provide good performance during nominal fine pointing but limits telescope capability to rapidly slew and acquire targets. On the other hand, the use of image motion compensation can substantially reduce pointing error at the end of a slew but is limited by attitude sensor noise when using high gain feedback.

Overall, body pointing plus image motion compensation potentially offers superior performance but must be judged against the difficulties posed by attitude sensor noise, the higher cost and complexity of secondary mirror control, and the acceptable fine-pointing performance provided by body pointing alone.

Additional study would require a higher fidelity structural model and detailed models of the attitude sensor and actuator. The most significant control problem is flexible mode suppression to minimize slew settling time. A combination of control compensation and command profile should be designed to optimize slew maneuvers. In addition, alternative attitude sensor designs that would permit use of IMC should be investigated. The benefits of IMC in removing disturbances seen by the attitude sensor may then be fully exploited.

Acknowledgment

This work was sponsored by the NASA Ames Research Center. The authors wish to acknowledge the contributions of T.E. Strikwerda, J.W. McIntyre, M.D. Griffin, and D.G. Grant of the Applied Physics Laboratory and K. Nishioka, J.P. Murphy, and L. Manning of NASA Ames.

References

[1] Nishioka, K. and Murphy, J.P., "Space Infrared Telescope Facility: Conceptual Spacecraft Definition," International Society for Optical Engineering.

[2] Griffin, M.D. et al., "Space Infrared Telescope Facility Pointing Control System Analysis," JHU/APL Report SDO-7434, Oct. 1984.

[3] Sperry Flight Systems Division, Control Moment Gyros Informational Brochure, May 1982.

[4] Kollodge, J.C. and Sand, J.A., "An Advanced Star Tracker Design Using the Charge Injection Device," Joint IFAC/ESA Symposium on Automatic Control in Space, Noorduijkerhout, The Netherlands, July 5-9, 1982.

[5] "Teledyne Specification for DRIRU II," Identification No. 17863, Drawing No. 7516544, Sheet 7, pp. 3-14.

[6] *Spacecraft Attitude Determination and Control*, edited by J. R. Wertz, Reidel, 1978.

[7] "Space Station ACS Technology Considerations," Sperry Corporation, Flight Systems Division, 1984.

[8] Gregory, C. Z., "Reduction of Large Flexible Models Using Internal Balancing Theory," 1983 AIAA Conference on Guidance and Control, Gatlinburg, TN, Aug. 15-17, pp. 805-814.

[9] Skelton, R.E., Hughes, P.C., and Hablani, H.B., "Order Reduction for Models of Space Structures Using Modal Cost Analysis," *Journal of Guidance and Control*, Vol. 5, July 1982, pp. 351-357.

[10] Yousuff, A. and Skelton, R. E., "Controller Reduction by Component Cost Analysis," *IEEE Transactions on Automatic Control*, Vol. AC-29, June 1984.

[11] Glaese, J.R., Kennel, H.F., Nurre, G.S., Seltzer, S.M., and Shelton, H.L., "Low-Cost Space Telescope Pointing Control System," *Journal of Spacecraft and Rockets*, Vol. 13, July 1976, pp. 400-405.

[12] Dougherty, H., Tompetrini, K., Levinthal, J., and Nurre, G., "Space Telescope Pointing Control System," *Journal of Guidance and Control*, July 1982, Vol. 5, pp. 403-409.

[13] Chiarappa, D.J., "Evaluation of Control Systems for Fine Pointing of Astronomy Spacecraft to 0.025 μrad (0.005 arcsec)," General Dynamics/Convair, San Diego, CA, CASD-ERR-73-006, Dec. 1973.

[14] Balas, M.J., "Some Trends in Large Space Structure Control Theory: Fondest Hopes; Wildest Dreams," *IEEE Transactions on Automatic Control*, Vol. AC-27, June 1982, pp. 522-535.

[15] Aubrun, J.N., "Theory of the Control of Structures by Low-Authority Controllers," *Journal of Guidance and Control*, Vol. 3, Sept. 1980, pp. 444–451.

[16] Turner, J.D., Chun, H.M., and Junkins, J.L., "Optimal Large-Angle Maneuvers with Vibration Suppression," *Workshop on Modeling, Analysis and Optimization Issues for Large Space Structures*, L.D. Pinson et al., Williamsburg, VA, Feb. 1983, pp. 177-215.

[17] Sridhar, B., Aubrun, J.N., Lorell, R.R., "Design of a Precision Pointing Control System for the Space Infrared Telescope Facility," *IEEE Control Systems Magazine*, Feb. 1986, pp. 28-34.